

Bio-inspired pneumatic shape-morphing elastomers

Emmanuel Siéfert, Etienne Reyssat, José Bico and Benoît Roman*

Shape-morphing structures are at the core of future applications in aeronautics¹, minimally invasive surgery², tissue engineering³ and smart materials⁴. However, current engineering technologies, based on inhomogeneous actuation across the thickness of slender structures, are intrinsically limited to one-directional bending⁵. Here, we describe a strategy where mesostructured elastomer plates undergo fast, controllable and complex shape transformations under applied pressure. Similar to pioneering techniques based on soft hydrogel swelling^{6–10}, these pneumatic shape-morphing elastomers, termed here as ‘baromorphs’, are inspired by the morphogenesis of biological structures^{11–15}. Geometric restrictions are overcome by controlling precisely the local growth rate and direction through a specific network of airways embedded inside the rubber plate. We show how arbitrary three-dimensional shapes can be programmed using an analytic theoretical model, propose a direct geometric solution to the inverse problem, and illustrate the versatility of the technique with a collection of configurations.

Morphing a thin plate into a programmed shape is a challenging problem, as highlighted by Gauss: if the distances along the surface are not modified, the Gaussian curvature cannot be changed, and only a limited family of three-dimensional (3D) surfaces is achievable, as commonly observed with bilayer sheets^{16,17}. However, nature overflows with examples of geometrically complex thin objects, such as leaves or organ epithelia¹¹. For instance, differential growth induces the elegant shape of flower petals¹², or may crinkle an initially flat leaf when the growth rate is deregulated¹³. While the growth process may be spatially homogeneous, the orientations of cellulose fibres may also induce anisotropic growth, which leads to the hygroscopic actuation of wheat awns¹⁴ or to the chiral shape of some seed pods¹⁵.

Inspired by biological morphogenesis, pioneering experiments have been carried out with hydrogel plates where inhomogeneous isotropic^{6,7,18} or anisotropic^{9,10} swelling properties are spatially distributed to obtain various 3D shapes after being immersed in a bath of hot water. Nevertheless, the experimental realizations developed so far involve slow diffusive swelling processes and very soft objects that generally cannot sustain their own weight. In contrast, pneumatic actuation presents strong advantages, such as large work load, reversibility, controllability and fast actuation, which have led to the recent development of multiple soft robotics actuators for twisting, contracting, expanding or bending motions¹⁹. However, such actuators generally rely on bilayers⁵ or are limited to surface texturing effects²⁰; this imposes strong constraints on the achievable states. Our approach bridges these two emerging fields—bio-inspired shape-morphing and pneumatic soft robotics—with a new easy-to-build, easy-to-control object, referred to as a baromorph.

Baromorphs consist of elastomer plates embedding a network of airways (see Methods for fabrication details), which give rise to a programmed family of shapes under air inflation or suction. Such structures can be viewed as pneumatic metamaterials²¹. When the inner pressure is increased (or decreased), the elongated channels tend to inflate (or deflate) anisotropically²². The length of an inflated channel remains almost unchanged, while its width increases (Fig. 1a). This anisotropy results in a controllable modification of the effective rest lengths of the baromorph, mimicking the anisotropic growth of a biological tissue, with a magnitude that depends on the geometry of the inner channels and on the applied pressure. The plate deforms according to the new target metric imposed by the network of airways, and may buckle out of plane to reach an equilibrium 3D shape that minimizes the total elastic energy (the sum of stretching and bending energies).

Figure 1c presents the deformation of a baromorph plate with radial channels obtained by casting the 3D printed template shown in Fig. 1b: the target expansion is mainly circumferential. Following suction and consequent azimuthal contraction, the plate adopts a bowl shape (with positive Gaussian curvature). Conversely, inflation induces an azimuthal expansion and leads to an excess angle in the plate, which destabilizes into a surface of negative Gaussian curvature. These transformations are reminiscent of the morphing evolution of *Acetabularia* (Fig. 1d)^{11,23}. After initiation, the cap of this unicellular alga evolves from a bowl to a flat configuration, and eventually to a saddle shape, essentially for the same reason as our baromorph: biological growth in the cap is stronger in the circumferential direction than along the radius.

A first step in understanding and programming a baromorph is to predict the local deformation of airways in the absence of external geometrical constraints, that is, the target in-plane strains orthogonal ϵ_{\perp}^t and parallel ϵ_{\parallel}^t to the airway direction. The channel geometry (Fig. 2a) can be reduced to two relevant parameters in our minimal model: the relative channel height with respect to the total thickness of the sheet $\Psi = h/(h + 2e)$ and the in-plane channel density $\Phi = d/(d + d_w)$, where h , e , d and d_w are geometrical parameters of the structure (Fig. 2b). Balancing stresses and making simplifying assumptions (for details see Supplementary Text and Supplementary Fig. 2), the target strains are then deduced following Hooke’s law:

$$\epsilon^t = \frac{p}{E} \frac{\Psi\Phi}{1 - \Psi\Phi} (1 - 2\nu) = 0$$

$$\epsilon_{\perp}^t = \frac{p}{E} (2 - \Phi) \Phi \left(\frac{\Psi}{1 - \Psi} - \frac{\nu\Psi\Phi}{1 - \Psi\Phi} \left[1 + \nu \left(\frac{1 - \Phi}{\Phi(1 - \Psi)} \right) \right] \right) \quad (1)$$

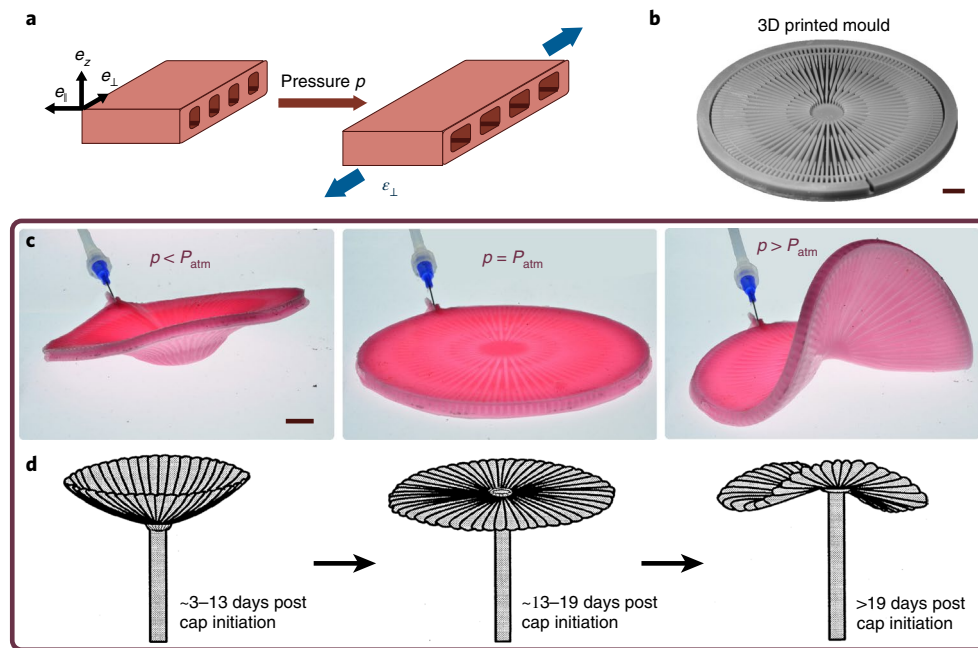


Fig. 1 | Principle of pressure-actuated baromorph plate. **a**, Schematic of actuation: the pressure inside the airways induces anisotropic inflation of the plate (higher strain normal to the airways than along the channels). **b**, 3D printed mould used to cast the baromorph illustrated in **c**. **c**, Actuation of the plate: suction (left) tends to contract the plate in the azimuthal direction, leading to a bowl (positive Gaussian curvature), while inflation (right) leads to an excess angle and a transformation into a saddle shape (negative Gaussian curvature). Scale bars, 1 cm. **d**, Evolution of the cap of an *Acetabularia* alga from a bowl to a saddle shape due to preferential growth in the azimuthal direction. Adapted from ref. ²³, Springer (**d**).

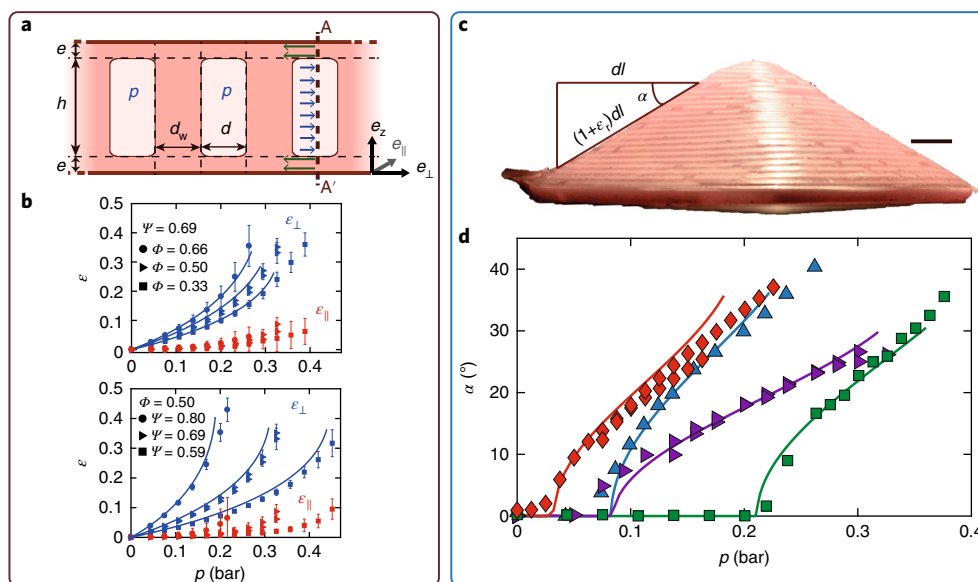


Fig. 2 | Characterization of baromorph expansion and deformation. **a**, Schematic vertical cut of the baromorph structure. The geometry of the channels can be reduced to two non-dimensional parameters: the relative height $\Psi = h/(h + 2e)$ and the channel density $\Phi = d/(d + d_w)$, where d is the width of the channels, d_w is the width of the walls, h is the height of the channels and e is the thickness of the covering membrane. **b**, Dependence of the targeted parallel and longitudinal strain on pressure for different values of Φ with $\Psi = 0.69 \pm 0.05$ and for different values of Ψ with $\Phi = 0.5 \pm 0.02$. Solid lines correspond to the model without any fitting parameter (in our simplified model ϵ_{\parallel} vanishes). **c**, Baromorph programmed to be a cone when pressurized. A radial segment of length dl in the rest state will elongate to $(1 + \epsilon_r)dl$ upon inflation, leading to a slope angle α . Scale bar, 1 cm. **d**, Experimental (symbols) and theoretical (solid lines, no fitting parameter) evolution of α as a function of applied pressure for baromorphs of different parameters: red diamonds ($\Psi = 0.78 \pm 0.05$, $\Phi = 0.5$, $R = 50$ mm, $H = 3.8 \pm 0.2$ mm); blue triangles ($\Psi = 0.74$, $\Phi = 0.5$, $R = 40$ mm, $H = 5.4$ mm); purple flags ($\Psi = 0.68$, $\Phi = 0.2$, $R = 50$ mm, $H = 6$ mm); green squares ($\Psi = 0.6$, $\Phi = 0.5$, $R = 40$ mm, $H = 6.7$ mm).

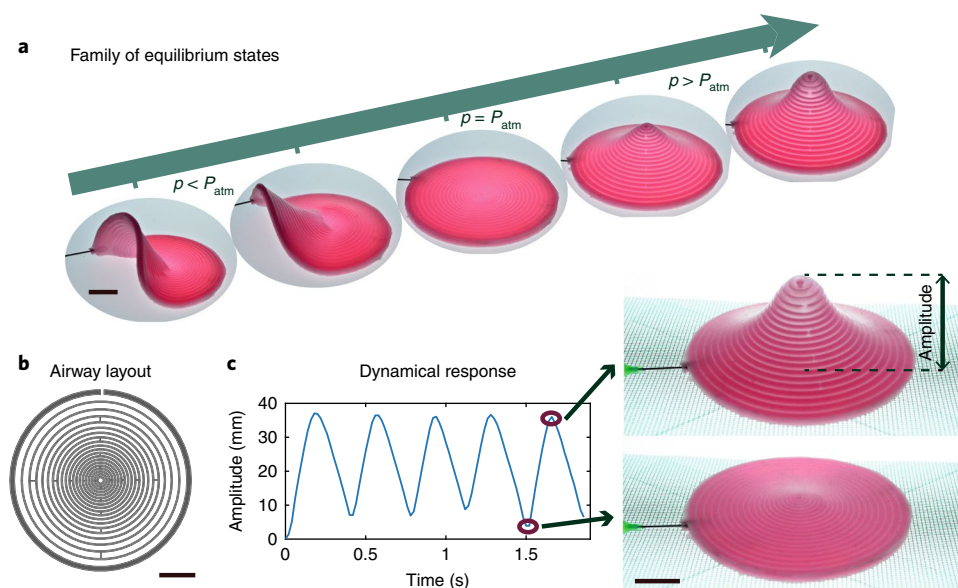


Fig. 3 | Equilibrium states and dynamical response. **a**, Continuous family of equilibrium states obtained for a baromorph under different pressures. **b**, Corresponding network of channels embedded in the plate. Channels are more concentrated in the central region of the disk, which leads to a spiky structure once inflated. **c**, Dynamical response: actuation at approximately 3 Hz of the pneumatic system (Supplementary Video 6). Scale bars, 2 cm.

where E and ν are Young's modulus and the Poisson ratio of the elastomer, respectively. We measured the target strains (Fig. 2b) by inflating a ring composed of only a few channels, therefore free of radial constraint. Within our crude hypotheses, the longitudinal strain is zero for $\nu = 1/2$, as expected for an incompressible elastomer, and we do observe that the longitudinal strain is much smaller than the transverse strain. We can account for the evolution of the parameters (Ψ , Φ) due to the deformation of the channels under pressure, as described in the Supplementary Information, and input the actual values into equation (1). The resulting nonlinear prediction for the target strain is in very good agreement with experimental data, without any fitting parameter, as illustrated in Fig. 2b (note that the calculations remain within the framework of Hookean linear elasticity: material stiffening at large strain is not considered in this simplified model).

We now employ the concept of the anisotropic target metric to program 3D shapes. As a first application, we targeted an axisymmetric shape, a cone. A configuration made of concentric and regularly spaced circular air channels is expected to induce a uniform radial target strain ϵ_r^t , while the azimuthal target strain remains null. Following elementary geometry (Fig. 2c), both target strains are satisfied if the airways keep their initial radii and the plate adopts a conical shape of slope α , with

$$\cos\alpha = \frac{1}{1 + \epsilon_r^t} \quad (2)$$

After a buckling transition, conical shapes with a tip regularized by the finite bending stiffness of the plate are observed for high applied pressures (Fig. 2d and Supplementary Fig. 4). As in traditional buckling of slender structures, the finite bending stiffness of the plate indeed prevents out-of-plane buckling for small strains²⁴ (Supplementary Fig. 5). Both the buckling threshold and the evolution of the angle can be rationalized when inserting the incompatible target strain from equation (1) within the Föppl–Von Karman equations for plates²⁵ (see Supplementary Text for a derivation and Supplementary Fig. 3).

In Fig. 2d, the results from numerical integration of these equations for incompatible plates without any fitting parameter are plotted

as solid lines, and match the experimental angles. Equation (1) is not limited to uniform channels, but is also valid locally if the channels' distribution follows a gradient. In the configuration illustrated in Fig. 3, the channel density decreases with the radius, which results in a spiky structure when inflated. Conversely, the channels tend to collapse under suction, leading to a negative value of ϵ_r^t . As a consequence, the structure adopts a saddle shape with negative Gaussian curvature, as theoretically predicted by Efrati and colleagues²⁵. A continuous family of shapes is thus obtained when adjusting the pressure. Each shape corresponds to an equilibrium state and can be easily reached on demand.

Another key advantage of baromorphs relies on their fast pneumatic actuation²⁶. In the example described in Fig. 3c, a reversible transformation of the plate could be achieved with a frequency of 3 Hz (Supplementary Video 1). The structures presented in this study have an initial diameter on the order of 10 cm and channels with a section close to 1 mm². Baromorphs are, however, not limited to this size. For a given shape of the structure, the static mechanical response is independent of scale (Supplementary Fig. 6 and Supplementary Video 2). Provided with a sufficient power input, the actuation velocity is, in this case, limited by the natural frequency of the plate, $\omega \sim h(E/\rho)^{1/2}/R^2$, where ρ is the elastomer density, leading to a typical frequency of 10 Hz. For small-scale structures, a poroelastic timescale could limit the actuation as in the context of water transport in plants²⁷. Conversely, the finite compressibility of air may be a limiting issue for large baromorph structures. The actuation principle is moreover largely material-independent, so that any elastomer may be used, including relatively stiff, tough and wear-resistant rubber, allowing metre-sized structures to resist their weight.

Having captured the mechanical ingredients involved in the transformation of a baromorph, we now explore shape-programming issues. Elementary shapes can be programmed through simple computations. For instance, purely radial (respectively azimuthal) growth of uniform intensity leads to a cone (respectively an e-cone¹¹, the surface obtained geometrically when inserting an angular sector in an initially flat disk). This is confirmed by baromorphs with entirely azimuthal (Fig. 4a) respectively radial (Fig. 4c) channels at constant channel density, which display zero Gaussian

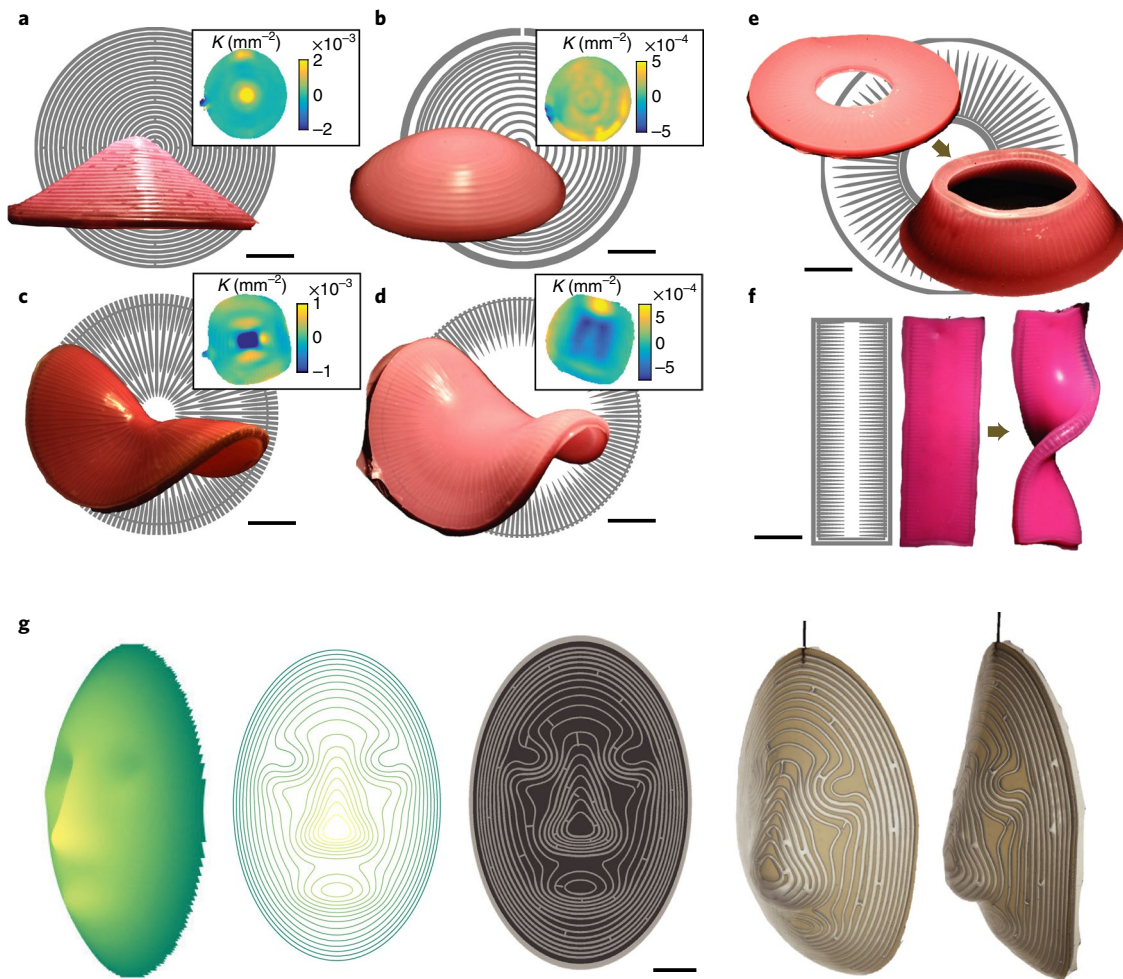


Fig. 4 | Collection of 3D shapes obtained by the buckling of baromorphs under pressure. a,b, Circular concentric channels: cone (**a**) and portion of a sphere (**b**). **c,d**, Radial channels: e-cone (**c**) and saddle (**d**). **e**, Truncated cone of large angle. **f**, Helicoid. Grey background paths represent the underlying airway network. Insets, plots of Gaussian curvature K . **g**, Shape programming of a face. From left to right: the target shape, the corresponding contour lines, the network of channels computed to give rise to the target metrics and two pictures of the deformed baromorph, made of Dragon Skin 10 Medium from Smooth-On. Videos of the transformations of most structures are available as Supplementary Videos 3–7). Scale bars, 2 cm.

curvature except at the apex (for details on the scanning technique see Methods and Supplementary Fig. 1).

A spherical cap with constant positive Gaussian curvature (Fig. 4b and Supplementary Video 3) is programmed by azimuthal channels with a density according to equation (2) with a varying value of angle $\alpha = \arcsin(r/R)$. As discussed in the Supplementary Information, less intuitive families of shapes can be simply obtained from the azimuthal growth of radial channels. Surfaces with constant negative Gaussian curvature may be programmed with radial channels with varying density (Fig. 4d and Supplementary Video 4). Figure 4e shows how a flat annulus almost becomes a cylinder, by expansion of the inner circumference (Supplementary Fig. 7a and Supplementary Video 5). Baromorphs are not limited to axisymmetric plates. For instance, a ribbon may spontaneously buckle into a helicoid, as expected when a larger target strain is programmed along the edges (Fig. 4f, Supplementary Fig. 7b and Supplementary Video 6).

Programming an arbitrary shape, however, involves a non-trivial inverse problem, as in other practical realizations of shape morphing. For instance, the direction of the anisotropic target growth (in nematic elastomers^{8,28}) or the isotropic growth factor (in swelling gels⁷ or auxetic materials²⁹) corresponding to a given target shape may only be computed through a numerical optimization

procedure with no formal guarantee for the existence of a solution. In the specific case of baromorphs, the possibility to select both the orientation and the density of the channels enables us to tune at each point both the direction and intensity of the local expansion. Taking advantage of this additional degree of freedom, we propose a straightforward and intuitive analytical recipe for programming a smooth surface that can be parametrized as $z = h(x, y)$. In this procedure, each point of the baromorph is moving along the z axis during activation, in a simple generalization of the axisymmetric case (Fig. 2c).

Contour lines (curves with equal h projected onto the reference plane $z = 0$) are conserved in the process, and no growth occurs along these curves, which we choose as the centreline for the baromorph channels. The local slope angle α measured on the target surface perpendicular to the contour lines, $\tan \alpha = \|\nabla h\|$, determines through equation (2) the lateral target strain

$$\epsilon_{\perp}^t = \sqrt{1 + \left(\frac{\partial h}{\partial x}\right)^2 + \left(\frac{\partial h}{\partial y}\right)^2} - 1 \quad (3)$$

which in turn sets the width of the airways (that is, Φ) for the desired pressure p using equation (1).

This arrangement ensures that, in the geometric limit (that is, for thin enough plates), the baromorph will follow the target metrics (Supplementary Text). Figure 4g shows the programming and realization of a face following the method described above. The results are qualitatively in good agreement with the target shape, except for the finest details (such as the eyes), which are smoothed out by bending elasticity (Supplementary Video 7). Indeed, the size of the eyes is of the same order as the thickness of the sheet, and bending rigidity cannot be neglected at this scale.

Baromorphs constitute an efficient and versatile tool to transform 2D sheets into complex 3D structures reversibly with fast actuation. Numerous extensions of this architected active material are possible for practical applications: cuts²⁹ can be made in the plate to release some bending constraints and improve the shape programming (Supplementary Fig. 8 and Supplementary Video 8). The target curvature tensor can also be programmed^{25,30} using a bilayer composed of two independent networks of airways. In such a configuration, the homogenized sheet is free of constraint and the actuation does not involve any threshold. Snapping instabilities can also be triggered with out-of-phase actuation of the layers, as shown in Supplementary Video 9. More generally, several intertwined networks may be embedded in one plate to program various shapes on demand. Rather than simple channels, controlled cavities with different sizes and shapes may be embedded in the plate to impose all three components of the target growth tensor, in contrast with current morphing techniques^{6,7,10,28} (Supplementary Fig. 9 and Supplementary Video 10). Altogether, our study opens pathways in the numerous areas where shape morphing is anticipated to find new innovative applications, such as minimally invasive surgery, bioprinting, flow optimization, architecture or more generally smart materials.

Online content

Any methods, additional references, Nature Research reporting summaries, source data, statements of data availability and associated accession codes are available at <https://doi.org/10.1038/s41563-018-0219-x>.

Received: 8 January 2018; Accepted: 9 October 2018;

Published online: 19 November 2018

References

1. Ajaj, R. M., Beaverstock, C. S. & Friswell, M. I. Morphing aircraft: the need for a new design philosophy. *Aerospace Sci. Technol.* **49**, 154–166 (2016).
2. Cianchetti, M. et al. Soft robotics technologies to address shortcomings in today's minimally invasive surgery: The stiff-flop approach. *Soft Robotics* **1**, 122–131 (2014).
3. Gao, B. et al. 4D bioprinting for biomedical applications. *Trends Biotechnol.* **34**, 746–756 (2016).
4. McEvoy, M. A. & Correll, N. Materials that couple sensing, actuation, computation, and communication. *Science* **347**, 1261689 (2015).
5. Shepherd, R. F. et al. Multigait soft robot. *Proc. Natl Acad. Sci. USA* **108**, 20400–20403 (2011).
6. Klein, Y., Efrati, E. & Sharon, E. Shaping of elastic sheets by prescription of non-Euclidean metrics. *Science* **315**, 1116–1120 (2007).
7. Kim, J., Hanna, J. A., Byun, M., Santangelo, C. D. & Hayward, R. C. Designing responsive buckled surfaces by half-tone gel lithography. *Science* **335**, 1201–1205 (2012).
8. Aharoni, H., Sharon, E. & Kupferman, R. Geometry of thin nematic elastomer sheets. *Phys. Rev. Lett.* **113**, 257801 (2014).
9. Erb, R. M., Sander, J. S., Grisch, R. & Studart, A. R. Self-shaping composites with programmable bioinspired microstructures. *Nat. Commun.* **4**, 1712 (2013).

10. Sydney Gladman, A., Matsumoto, E. A., Nuzzo, R. G., Mahadevan, L. & Lewis, J. A. Biomimetic 4D printing. *Nat. Mater.* **15**, 416–418 (2016).
11. Dervaux, J. & Ben Amar, M. Morphogenesis of growing soft tissues. *Phys. Rev. Lett.* **101**, 068101 (2008).
12. Rebocho, A. B., Kennaway, J. R., Bangham, J. A. & Coen, E. Formation and shaping of the antirrhinum flower through modulation of the cup boundary gene. *Curr. Biol.* **27**, 2610–2622 (2017).
13. Nath, U., Crawford, B., Carpenter, R. & Coen, E. Genetic control of surface curvature. *Science* **299**, 1404–1407 (2003).
14. Fratzl, P., Elbaum, R. & Burgert, I. Cellulose fibrils direct plant organ movements. *Faraday Discuss.* **139**, 275–282 (2008).
15. Armon, S., Efrati, E., Kupferman, R. & Sharon, E. Geometry and mechanics in the opening of chiral seed pods. *Science* **333**, 1726–1730 (2011).
16. Reyssat, E. & Mahadevan, L. Hygromorphs: from pine cones to biomimetic bilayers. *J. R. Soc. Interface* **6**, 951–957 (2009).
17. Pezzulla, M., Smith, G. P., Nardinocchi, P. & Holmes, D. P. Geometry and mechanics of thin growing bilayers. *Soft Matter* **12**, 4435–4442 (2016).
18. Huang, L. et al. Ultrafast digital printing toward 4D shape changing materials. *Adv. Mater.* **29**, 1605390 (2017).
19. Gorissen, B. et al. Elastic inflatable actuators for soft robotic applications. *Adv. Mater.* **29**, 1604977 (2017).
20. Pikul, J. H. et al. Stretchable surfaces with programmable 3D texture morphing for synthetic camouflaging skins. *Science* **358**, 210–214 (2017).
21. Bertoldi, K., Vitelli, V., Christensen, J. & van Hecke, M. Flexible mechanical metamaterials. *Nat. Rev. Mater.* **2**, 17066 (2017).
22. Timoshenko, S. & Woinowsky-Krieger, S. *Theory of Plates and Shells* 2nd edn (McGraw-Hill, New York, 1959).
23. Serikawa, K. A. & Mandoli, D. F. An analysis of morphogenesis of the reproductive whorl of *Acetabularia acetabulum*. *Planta* **207**, 96–104 (1998).
24. Dias, M. A., Hanna, J. A. & Santangelo, C. D. Programmed buckling by controlled lateral swelling in a thin elastic sheet. *Phys. Rev. E* **84**, 036603 (2011).
25. Efrati, E., Sharon, E. & Kupferman, R. Elastic theory of unconstrained non-Euclidean plates. *J. Mech. Phys. Solids* **57**, 762–775 (2009).
26. Mosadegh, B. et al. Pneumatic networks for soft robotics that actuate rapidly. *Adv. Funct. Mater.* **24**, 2163–2170 (2014).
27. Dumais, J. & Forterre, Y. 'Vegetable dynamics': the role of water in plant movements. *Annu. Rev. Fluid. Mech.* **44**, 453–478 (2012).
28. Aharoni, H., Xia, Y., Zhang, X., Kamien, R. & Yang, S. Universal inverse design of surfaces with thin nematic elastomer sheets. *Proc. Natl Acad. Sci. USA* **115**, 7206–7211 (2018).
29. Konakov, M. et al. Beyond developable: computational design and fabrication with auxetic materials. *ACM Trans. Graph.* **35**, 1–11 (2016).
30. van Rees, W. M., Vouga, E. & Mahadevan, L. Growth patterns for shape-shifting elastic bilayers. *Proc. Natl Acad. Sci. USA* **114**, 11597–11602 (2017).

Acknowledgements

This work received support from the Institut Pierre-Gilles de Gennes (Équipement d'excellence, 'investissements d'avenir', ANR-10-EQPX-34) and from ANR SMART. The authors thank C. Blanquart for developing the 3D scanning technique and M. Lebihain from the Institut Jean Le Rond d'Alembert for technical support with 3D printing of the moulds.

Author contributions

E.S. and B.R. developed the baromorph concept. E.S. designed and conducted the experiments. E.S., E.R., J.B. and B.R. analysed the data. E.S., J.B. and B.R. developed the theoretical model. All authors participated in editing of the manuscript.

Competing interests

The authors declare no competing interests.

Additional information

Supplementary information is available for this paper at <https://doi.org/10.1038/s41563-018-0219-x>.

Reprints and permissions information is available at www.nature.com/reprints.

Correspondence and requests for materials should be addressed to B.R.

Publisher's note: Springer Nature remains neutral with regard to jurisdictional claims in published maps and institutional affiliations.

© The Author(s), under exclusive licence to Springer Nature Limited 2018

Methods

Making baromorph plates. The baromorph plates were made of polyvinyl siloxane (Elite Double 8 from Zhermack or Dragon Skin 10 Medium from Smooth-On) by mixing equal quantities of catalyst and base liquids. The mixture was then poured onto a 3D printed mould designed using OpenScad software and printed with a Form2 printer from Formlabs. If necessary, the entire set-up was placed in a vacuum chamber to efficiently remove trapped air bubbles. Curing required, respectively, 20 min and 3 h. At the same time, a sheet of thickness e of the same elastomer was spread on a flat surface and cured. The structure removed from the mould was finally closed by ‘gluing’ the flat sheet on top of the moulded sheet using a thin layer of uncured mixture of the same material.

Experimental strain data. Azimuthal and radial strains were measured experimentally using a digital image correlation (DIC) program, CorreliQ4, on Matlab³¹. A random pattern of dots was generated on the surface by spraying paint. Top-view pictures of the baromorph structure were taken at different pressures and the program tracked in-plane strain with respect to a chosen reference image. Mean strains perpendicular and parallel to the channels were then extracted.

3D scanning and computation of Gaussian curvature. The surface topography of inflated baromorph structures was measured with a 3D scanning system developed in the laboratory and based on the work of Cobelli and colleagues³². Basically, the 3D shape was inferred from the distortion of a pattern of stripes projected on the structure (Supplementary Fig. 1a,b). The local height was thus deduced from the phase shift of the periodic pattern.

Although Fourier transform is generally used to extract the phase, the lack of periodic boundaries prevented us from using this method. We instead used a phase shifting profilometry technique, as detailed in ref. ³³. Four patterns were successively projected and recorded with the camera, each time shifted by $\pi/2$. The local phase $\varphi(x,y)$ could thus be directly computed as

$$\varphi(x,y) = \arctan\left(\frac{I_4 - I_2}{I_3 - I_1}\right) \quad (4)$$

where I_{1-4} are the local fringe intensities at pixel (x,y) for the different phase-shifted patterns. The local phase was defined at each pixel modulo π , then unwrapped using a 2D unwrap Matlab code written by M.F. Kasim (2D Weighted Phase Unwrapping) based on the work of Ghiglia and Romero³⁴. The local surface height can be deduced from the phase shift with respect to reference image $\Delta\varphi(x,y)$ using basic geometrical optics:

$$h(x,y) = \frac{\Delta\varphi L}{\Delta\varphi - 2\pi D/t} \quad (5)$$

where $\Delta\varphi = \varphi(x,y) - \varphi_0(x,y)$, D is the distance between the video projector and camera, L is the height of both instruments with respect to the flat surface of the reference, and t is the spatial wavelength of the fringed pattern (Supplementary Fig. 1c). The Gaussian curvature was finally deduced from a local quadratic fit of the surface (Supplementary Fig. 1d).

Data availability

The data supporting the findings of this study are available within the paper and its Supplementary Information files and from the corresponding author upon reasonable request.

References

- Hild, F. & Roux, S. Digital image correlation: from displacement measurement to identification of elastic properties—a review. *Strain* **42**, 69–80 (2006).
- Cobelli, P. J., Maurel, A., Pagneux, V. & Petitjeans, P. Global measurement of water waves by Fourier transform profilometry. *Exp. Fluids* **46**, 1037–1047 (2009).
- der Jeught, S. V., Soons, J. A. M. & Dirckx, J. J. J. Real-time microscopic phase-shifting profilometry. *Appl. Opt.* **54**, 4953–4959 (2015).
- Ghiglia, D. C. & Romero, L. A. Robust two-dimensional weighted and unweighted phase unwrapping that uses fast transforms and iterative methods. *J. Opt. Soc. Am. A* **11**, 107–117 (1994).